

Interfacial superconductivity and a Se-vacancy ordered insulating phase in the FeSe/PbO_x heterostructures

Yunkai Guo^{1,2}, Xuanyu Long³, Jingming Yan^{1,2}, Zheng Liu⁴, Qi-Kun Xue^{1,2,5,6*} and Wei Li^{1,2,7†}

¹State Key Laboratory of Low-Dimensional Quantum Physics, Department of Physics, Tsinghua University, Beijing 100084, China

²Frontier Science Center for Quantum Information, Beijing 100084, China

³Institute for Advanced Study, Tsinghua University, Beijing 100084, China

⁴School of Physics, Beihang University, Beijing 100191, China

⁵Beijing Academy of Quantum Information Sciences, Beijing 100193, China

⁶Southern University of Science and Technology, Shenzhen 518055, China

⁷Hefei National Laboratory, Hefei 230088, China

ABSTRACT. The discovery of high-temperature superconductivity in FeSe/SrTiO₃ has sparked significant interests in exploring new superconducting systems with engineered interfaces. Here, using molecular beam epitaxy growth, we successfully fabricate FeSe/PbO_x heterostructures and discover superconductivities in three different monolayer FeSe-related interfaces. We observe superconducting gaps of 13~14 meV in the monolayer FeSe films grown on two different phases of PbO_x. Moreover, we discover a new insulating Fe₁₀Se₉ phase with an ordered $\sqrt{5} \times \sqrt{5}$ Se-vacancy structure. Our first-principles calculation suggests that this new insulating phase originates from electronic correlation. Intriguingly, an additional monolayer FeSe film grown on the insulating Fe₁₀Se₉ also exhibits superconductivity with the gap size of 5 meV. Our results suggest that the work function differences between the monolayer FeSe and the substrates, which can induce band bending and charge transfer, are crucial for the interfacial superconductivity.

I. INTRODUCTION.

The discovery of the interfacial superconductivity in monolayer FeSe film grown on SrTiO₃ (FeSe/STO) [1] has opened a new avenue for the development of high-temperature superconductors. The superconducting gap closing temperature (T_{gc}) in FeSe/STO can reach as high as 83 K [1-6]. In addition to superconductivity, various novel phases, such as nematicity [3,7] and stripe order [8,9], have also been observed in FeSe/STO.

The influence of different substrates on superconductivity has been extensively studied [10-15]. For instance, the T_{gc} of monolayer FeSe on BaTiO₃ can reach up to 75 K [10,11]. In monolayer FeSe grown on anatase TiO₂, the measured superconducting gap can reach 21 meV, even slightly larger than that in FeSe/SrTiO₃ [12]. Enhanced superconductivity has also been reported in monolayer FeSe grown on the substrates other than TiO₂ terminations, such as MgO [13], GaO [14] and FeO [15]. Substrates play two key roles for the superconductivity. First, they provide sufficient charge carriers to monolayer FeSe and renormalize the

band structures topology of FeSe [2,3,16]. Second, they offer an additional electron-phonon coupling channel, characterized by the shake-off bands observed in ARPES measurements [10,17]. However, the mechanism of charge transfer from the substrate to FeSe remains controversial. Possible mechanisms include oxygen vacancies-induced doping [18] and work function-related band-bending effects [19].

As a typical band insulator, α -PbO shares an identical crystal structure with FeSe, but its in-plane lattice constants ($a = b = 3.99 \text{ \AA}$) are larger than those of both STO and FeSe. Here, we use molecular beam epitaxy to grow monolayer PbO_x on STO(001), and subsequently deposit few-layer FeSe films on PbO_x. Enhanced superconductivities are observed in monolayer FeSe/PbO_x. Additionally, we discover a new insulating Fe₁₀Se₉ phase with an ordered $\sqrt{5} \times \sqrt{5}$ Se-vacancy structure. Interestingly, superconducting gaps are also observed in an additional monolayer FeSe film grown on $\sqrt{5} \times \sqrt{5}$ Fe₁₀Se₉. These findings offer further insight into the charge transfer mechanism in monolayer FeSe-related systems.

II. EXPERIMENTAL METHODS

*Contact author: qkxue@mail.tsinghua.edu.cn

†Contact author: weili83@tsinghua.edu.cn

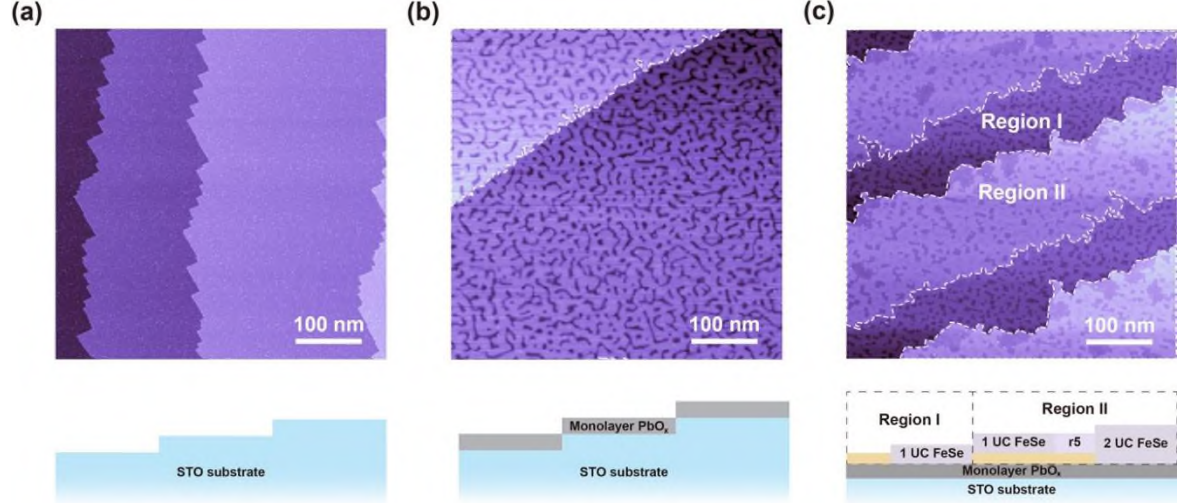


FIG. 1. The growth of FeSe/PbO_x on SrTiO₃(001). (a) STM topographic image of treated SrTiO₃(001) substrate (500 nm × 500 nm, $V_b = 2$ V, $I_t = 20$ pA). Flat substrate terraces can be observed. The lower panel is the schematic side view of STO. The shape of the steps corresponds to the terraces of STO. (b) STM topography of an insulating PbO_x monolayer film on SrTiO₃(001) (500 nm × 500 nm, $V_b = 7$ V, $I_t = 20$ pA). Its thickness is 400 pm. The step indicated by white dashed line in the topography is the terrace of the STO itself. The lower panel is the side view of PbO_x/STO. (c) Two distinct regions of monolayer FeSe/PbO_x (500 nm × 500 nm, $V_b = 2$ V, $I_t = 20$ pA). The lower panel is the side view of FeSe/PbO_x. Two regions are separated by black dotted lines.

The Nb-doped (0.05 wt%) STO (001) substrates were degassed in an ultrahigh vacuum chamber (base pressure is better than 3×10^{-10} Torr) at 500 °C for several hours and subsequently annealed at 1150 °C for 20 min to obtain TiO₂ terminated surface. To prepare PbO_x films, STO substrates were kept at 450 °C, and high purity Pb (99.999%) sources were evaporated by a Knudsen cell. High purity Fe (99.995%) and Se (99.9999%) sources were co-evaporated by two Knudsen cells to grow FeSe films. During the growth, the PbO_x/STO were kept at 430 °C. The as-grown samples were annealed at 430 °C for one hour to improve the sample quality.

In-situ STM measurements were performed at 4.8 K in a commercial STM (Unisoku). A polycrystalline PtIr STM tip was calibrated on an Ag island before STM experiments. STS data were taken by a standard lock-in method. The feedback loop is disrupted during data acquisition with the frequency of oscillation signal of 973.0 Hz.

All of the DFT calculations are obtained by using the Vienna ab initio Simulation Package (VASP)[20]. A freestanding single layer of Fe₁₀Se₉ unit cell with $\sqrt{5} \times \sqrt{5}$ Se vacancy order is constructed with STM measured in-plane lattice constant 8.7 Å and a vacuum layer of 15 Å. All of the internal ion positions are relaxed until the residual forces are less than 10^{-2} eV/Å.

The plane-wave cutoff is 500 eV in combination with the projector augmented wave (PAW) method [21]. The Monkhorst-Pack k-point grid [22] is $8 \times 8 \times 1$. The exchange and correlation is treated by using the Perdew-Burke-Ernzerhof generalized gradient approximation (GGA) functional [20]. The convergence criteria is 10^{-5} eV for electronic iterations. The rotational invariant $+U$ correction introduced by Dudarev et al. [21] with $U = 2$ eV is used for the DFT+U calculations. For the DOS calculation, the tetrahedron method with Blöchl corrections [22] is used with a $16 \times 16 \times 1$ k-point grid. Afterwards, the DOS is smoothed by convolution with an 8 meV-variance Gaussian function.

III. RESULTS

Figure 1(a) shows the topography of treated STO, revealing large, flat terraces. To aid in understanding the sample preparation, schematic side views are provided in the lower panel of Fig. 1. Oxygen atoms emitted by heating STO [12,23] combine with Pb atoms evaporated from a Knudsen cell, forming monolayer PbO_x on STO surface [see Fig. 1(b)]. By adjusting the temperatures of both the substrate and the Pb source, we can achieve the coverage of the monolayer PbO_x film up to 72%. The details for the growth process are shown in Fig. S1[24]. The height

*Contact author: qkxue@mail.tsinghua.edu.cn

† Contact author: weili83@tsinghua.edu.cn

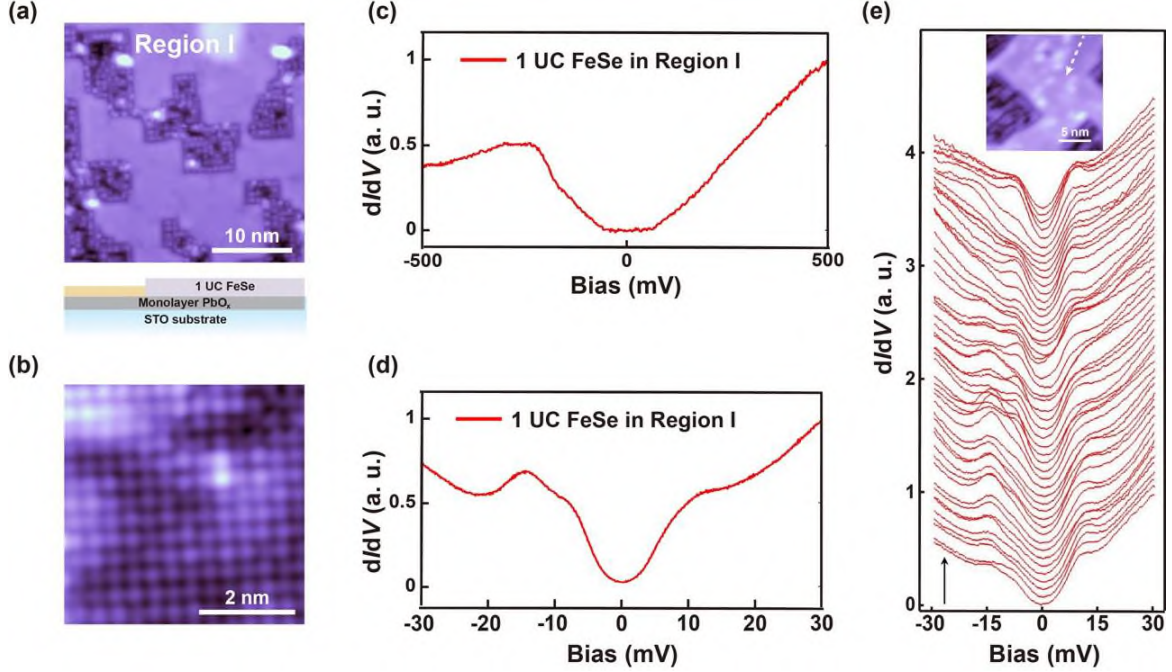


FIG. 2. Superconducting monolayer FeSe film grown on PbO_x . (a) STM topographic image of Region I ($30 \text{ nm} \times 30 \text{ nm}$, $V_b = 2 \text{ V}$, $I_t = 20 \text{ pA}$). The darker and rougher areas are another insulating phase, while the flatter areas are the monolayer FeSe. The lower panel is the schematic side view of Region I. The dark and rough areas are in yellow, while 1UC FeSe are in purple. (b) Atomically resolved STM topography of monolayer FeSe in Region I ($5 \text{ nm} \times 5 \text{ nm}$, $V_b = 100 \text{ mV}$, $I_t = 20 \text{ pA}$). (c) Large-scale dI/dV spectrum of the monolayer FeSe in Region I ($V_b = 500 \text{ mV}$, $I_t = 200 \text{ pA}$). (d) Typical low energy dI/dV spectrum ($V_b = 30 \text{ mV}$, $I_t = 200 \text{ pA}$). The superconducting gap is about 14 meV. (e) A series of low-energy dI/dV spectra ($V_b = 30 \text{ mV}$, $I_t = 200 \text{ pA}$) taken along the white arrow in inset. Inset: STM topography of Region I ($18 \text{ nm} \times 18 \text{ nm}$, $V_b = 2 \text{ V}$, $I_t = 20 \text{ pA}$).

of the monolayer PbO_x is 400 pm. The band gap size of PbO_x can be various, ranging from 1.5 to 4.2 eV [25-28]. For our STM measurements, stable scanning is only achievable when the bias voltage is higher than 7 V. Obtaining atomic resolution is challenging due to the insulating nature of the PbO_x film. Subsequently, FeSe films are grown on top of the PbO_x layer [Fig.1(c)]. Two distinct regions are observed in FeSe/ PbO_x [see Fig. 1(c)]. Region I is mostly monolayer FeSe, while Region II is more complex and will be discussed in detail later.

We first focus on Region I. Its topography and schematic side view are shown in Fig. 2(a). The flat areas consist of monolayer FeSe grown on PbO_x , where tetragonal lattice is observed [Fig. 2(b)]. Since STO is not completely covered by PbO_x , some rougher and insulating areas [the lower parts in Fig. 2(a)] are visible and they may have different stoichiometry, as indicated by the yellow sections in the schematic in the lower panel of Fig. 2(a). The STS looks flat and lacks DOS for a large bias range $\pm 60 \text{ mV}$, consistent with

prior literature reports [11,29-33]. This indicates that the hole pocket near the Γ point lies below the Fermi level, suggesting that electrons transfer from the substrate to 1 UC FeSe [2]. The superconducting gap of monolayer FeSe/ PbO_x can reach 14 meV [Fig. 2(d)]. Due to the limited quality of the FeSe/ PbO_x interface, the gaps fluctuate [Fig. 2(e)].

Now we focus on Region II, where four different FeSe phases are observed [Fig. 3(a)]. The areas labeled as 2 unit cell (UC) FeSe are 550 pm (the height of 1 UC FeSe) higher than the monolayer FeSe in Region I, indicating that they are 2 UC FeSe grown on the PbO_x [see the schematic in the lower panel of Fig. 3(a)]. The electronic structure of 2 UC FeSe is similar to that of 2 UC FeSe/STO (Fig. S2 [24]). The stripe charge order is rather weak due to the small size of the nematic domains (Fig. S3 [24]). In the mixture areas, 1 UC and 2 UC FeSe are interspersed (see Fig. S4 [24]).

The 1 UC FeSe in Region II is positioned higher than the 1 UC FeSe in Region I. As a result, the 1 UC FeSe here (purple layer) is located on the insulating

*Contact author: qkxue@mail.tsinghua.edu.cn

† Contact author: weili83@tsinghua.edu.cn

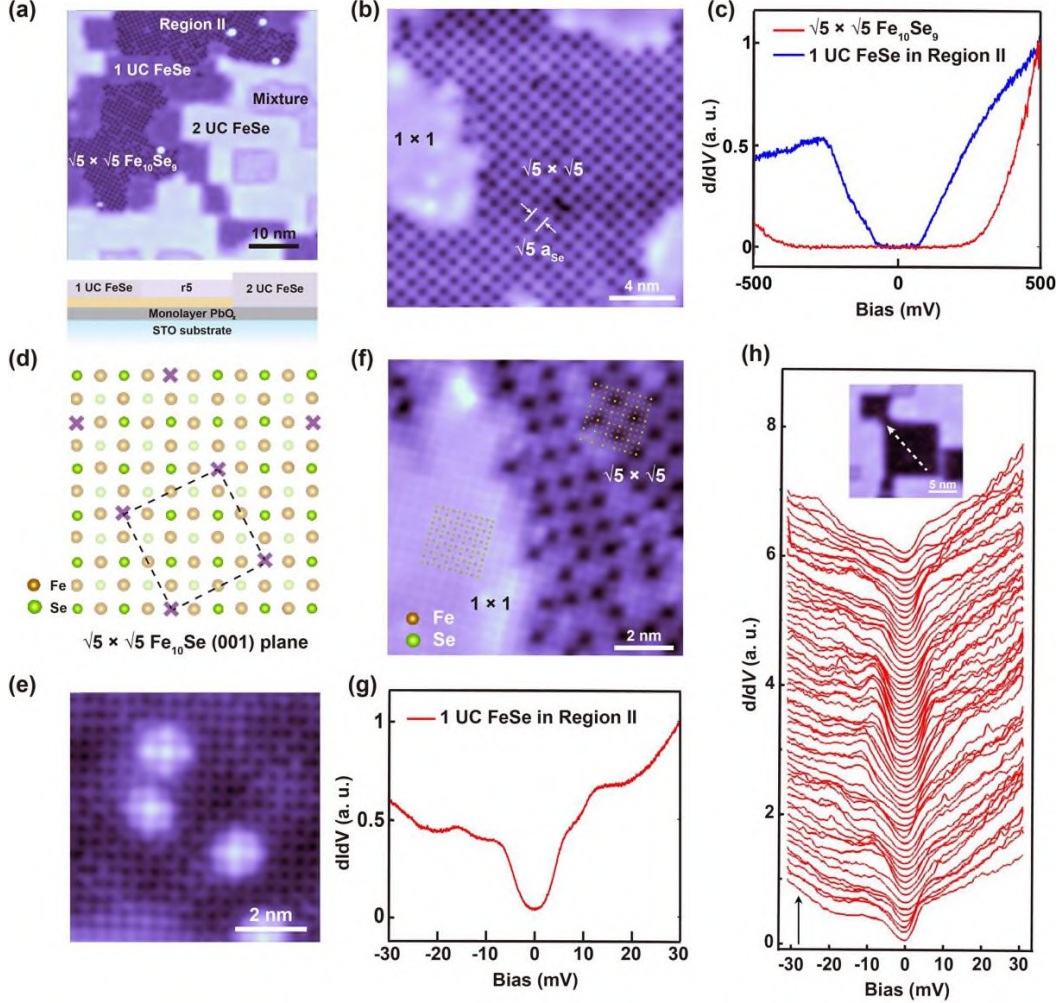


FIG. 3. Different phases in Region II. (a) STM topography of Region II ($50 \text{ nm} \times 50 \text{ nm}$, $V_b = 2 \text{ V}$, $I_t = 20 \text{ pA}$), in which four types of FeSe can be observed. The lower panel is the schematic side view of Region II. The “r5” represents $\sqrt{5} \times \sqrt{5} \text{ Fe}_{10}\text{Se}_9$. The mixture phase is omitted in the schematic. (b) Zoom-in STM topography of $\sqrt{5} \times \sqrt{5} \text{ Fe}_{10}\text{Se}_9$ and $1 \times 1 \text{ FeSe}$ in Region II ($18 \text{ nm} \times 18 \text{ nm}$, $V_b = 3.5 \text{ V}$, $I_t = 20 \text{ pA}$). The grid-like morphology corresponds to the $\sqrt{5} \times \sqrt{5} \text{ Fe}_{10}\text{Se}_9$ structure, while the flat surface corresponds to FeSe. The spacing between the grids is $\sqrt{5}$ times the lattice constant of Se a_{Se} . (c) dI/dV spectrum ($V_b = 500 \text{ mV}$, $I_t = 200 \text{ pA}$) of the $\sqrt{5} \times \sqrt{5}$ and 1×1 phase. Compared to the 1×1 phase, the $\sqrt{5} \times \sqrt{5}$ phase exhibits significantly pronounced insulating characteristics. (d) The structure of the $\sqrt{5} \times \sqrt{5}$ Se-vacancy pattern as seen from (001) planes. The topmost Se atoms are in green, while the lowermost Se atoms are in light green. The middle Fe atoms are in brown. The positions of Se vacancies are marked by purple crosses, which form $\sqrt{5} \times \sqrt{5}$ order. A unit cell is marked by the black dashed lines, which means that $\sqrt{5} \times \sqrt{5} \text{ Fe}_{10}\text{Se}_9$ phase corresponds to $\text{Fe}_{10}\text{Se}_9$. (e) Atomically resolved STM topography of monolayer FeSe in region II ($7 \text{ nm} \times 7 \text{ nm}$, $V_b = -10 \text{ mV}$, $I_t = 20 \text{ pA}$). Defects can be observed. (f) Atomically resolved STM topography of monolayer FeSe and $\sqrt{5} \times \sqrt{5} \text{ Fe}_{10}\text{Se}_9$ ($10 \text{ nm} \times 10 \text{ nm}$, $V_b = -3 \text{ V}$, $I_t = 20 \text{ pA}$) on Region II. 1×1 monolayer FeSe phase and $\sqrt{5} \times \sqrt{5} \text{ Fe}_{10}\text{Se}_9$ phase coexist. In the superposed schematic lattice, Fe atoms are in brown, while Se atoms are in green. Square lattices are formed by the topmost Fe and Se atoms. Se-vacancies (the black holes) form the $\sqrt{5} \times \sqrt{5}$ order. (g) Typical low energy dI/dV spectrum ($V_b = 30 \text{ mV}$, $I_t = 200 \text{ pA}$). The superconducting gap is about 13 meV . (h) A series of spectra taken along the white arrow in inset ($V_b = 30 \text{ mV}$, $I_t = 200 \text{ pA}$). The superconductivity is not uniform due to the sample quality. Inset: STM topography of a large area of monolayer FeSe in region II ($20 \text{ nm} \times 20 \text{ nm}$, $V_b = 2.5 \text{ V}$, $I_t = 20 \text{ pA}$). The dark areas are monolayer FeSe, while the light areas are 2 UC FeSe.

*Contact author: qkxue@mail.tsinghua.edu.cn

† Contact author: weili83@tsinghua.edu.cn

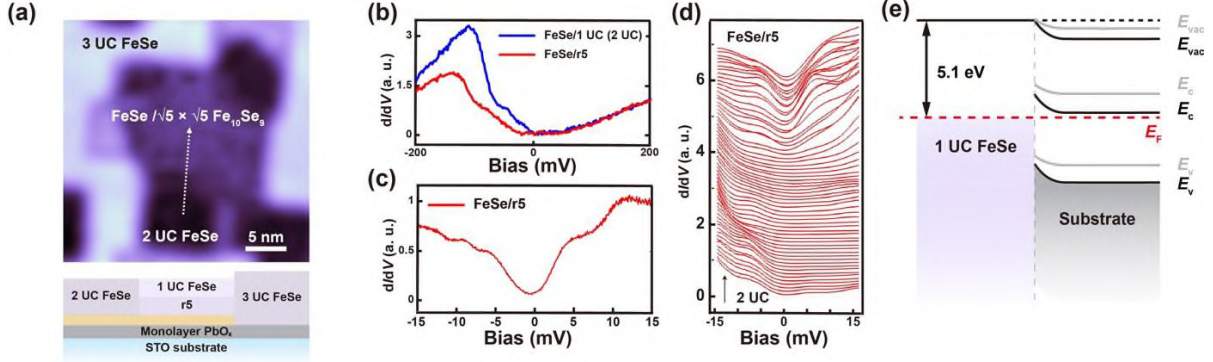


FIG. 4. Topography and electronic structures of additional monolayer FeSe layers grown on Region II. (a) STM topography ($30 \text{ nm} \times 30 \text{ nm}$, $V_b = 2 \text{ V}$, $I_t = 20 \text{ pA}$) after depositing additional FeSe layers on Region II, in which three types of FeSe (2 UC FeSe, FeSe/ $\sqrt{5} \times \sqrt{5} \text{ Fe}_{10}\text{Se}_9$ and 3 UC FeSe) can be observed. The schematic diagram in lower panel is the side view of FeSe/Region II. The “r5” represents $\sqrt{5} \times \sqrt{5} \text{ Fe}_{10}\text{Se}_9$. (b) Large-scale dI/dV spectra of the 2 UC and FeSe/ $\sqrt{5} \times \sqrt{5} \text{ Fe}_{10}\text{Se}_9$ phase ($V_b = 500 \text{ mV}$, $I_t = 200 \text{ pA}$). The dI/dV of FeSe/r5 has a flatter bottom near Fermi level than that in 2 UC FeSe. (c) Small-scale dI/dV spectrum ($V_b = 15 \text{ mV}$, $I_t = 200 \text{ pA}$) of the FeSe/ $\sqrt{5} \times \sqrt{5} \text{ Fe}_{10}\text{Se}_9$ phase, showing superconducting-like behaviors. (d) A series of dI/dV spectra with low energy ranges taken along the white arrow in **a** ($V_b = 15 \text{ mV}$, $I_t = 200 \text{ pA}$). A gap feature can be observed in FeSe/ $\sqrt{5} \times \sqrt{5} \text{ Fe}_{10}\text{Se}_9$ phase. (e) The band-bending effect in the interfaces between 1 UC FeSe and different substrates. The bands denoted by black lines have more remarkable band-bending effect than the gray ones.

layer mentioned earlier [the yellow layer in the schematic side views in Fig. 1(c) and 3(a)]. Notably, the 1 UC FeSe here also exhibits superconductivity, with a gap size of 13 meV [Fig. 3(g) and Fig. 3(h)].

In addition, we identified a new insulating phase in Region II, denoted as Fe₁₀Se₉, with an ordered $\sqrt{5} \times \sqrt{5}$ Se-vacancy structure. In Figure 3(b), the grid-like pattern is associated with the $\sqrt{5} \times \sqrt{5} \text{ Fe}_{10}\text{Se}_9$ structure, whereas the flat surface is characteristic of FeSe. Atomic-resolution images of both 1 UC FeSe and $\sqrt{5} \times \sqrt{5} \text{ Fe}_{10}\text{Se}_9$ are obtained in Fig. 3(f). The left side of Fig. 3(f) displays the 1×1 Se-lattice of 1 UC FeSe. While on the right side, the black holes correspond to the Se-vacancies arranged in a $\sqrt{5} \times \sqrt{5}$ order. In the schematic plot [Fig. 3(d)], purple crosses indicate the Se-vacancies, with the distance between the nearest vacancies $\sqrt{5}$ times the lattice constant of Se atoms. In contrast to the 1×1 phase, a large insulating gap is observed in the tunneling spectrum of the $\sqrt{5} \times \sqrt{5}$ phase [Fig. 3(c)]. As shown in Fig. S5 of the Supplemental Material [24], the Fe₁₀Se₉ phase exhibits distinct vacancy characteristics, contrasting with prior reports [34]: (1) Se vacancies form stable $\sqrt{5} \times \sqrt{5}$ ordered structures under varying bias voltages [Fig. S5(a)], confirming their morphological origin rather than electronic effects; (2) Isolated Fe vacancies are also observed (Fig. S5(b) and (c), where missing Fe atoms (red markers) expose their bonded topmost Se

atoms. These dual signatures unambiguously identify the Fe₁₀Se₉ phase.

We deposit an additional monolayer FeSe on Region II, and the original 1 UC FeSe and $\sqrt{5} \times \sqrt{5} \text{ Fe}_{10}\text{Se}_9$ become 2 UC FeSe and 1 UC FeSe/ $\sqrt{5} \times \sqrt{5} \text{ Fe}_{10}\text{Se}_9$, respectively [Fig. 4(a)]. Large-scale dI/dV spectra of the 2 UC FeSe and 1 UC FeSe/ $\sqrt{5} \times \sqrt{5} \text{ Fe}_{10}\text{Se}_9$ are of similar shape [Fig. 4(b)], while the DOS of FeSe/ $\sqrt{5} \times \sqrt{5} \text{ Fe}_{10}\text{Se}_9$ near E_F is flatter, which has similar tendency as the spectra shown in Fig. 2(c) and Fig. 3(c), indicating higher electron doping. Consistently, low-energy spectrum in 1UC FeSe/ $\sqrt{5} \times \sqrt{5} \text{ Fe}_{10}\text{Se}_9$ shows a superconducting-like gap [Fig. 4(c)]. The tunneling spectra [Fig. 4(d)] taken along the white arrowed dashed line in Fig. 4(a) indicate that the gap-like feature can be only observed in FeSe/ $\sqrt{5} \times \sqrt{5} \text{ Fe}_{10}\text{Se}_9$, but absent in 2 UC FeSe (i.e., 1 UC FeSe/FeSe).

IV. DISCUSSION AND CONCLUSIONS

We now discuss the potential origin of the charge transfer to monolayer FeSe. In total, we have discovered superconductivities in three monolayer FeSe-related interfaces. The observed DOS suppression is attributed to a superconducting gap as supported by the following evidence detailed in the Supplementary Materials [24]: (1) magnetic field-induced gap suppression in Regions I/II [Fig. S6 (d)–(e)]; (2) zero-bias current nulling (-1.5 to $+1.5 \text{ mV}$) in I - V curves [Fig. S6 (a)–(c)]; (3) persistent DOS

*Contact author: gqxue@mail.tsinghua.edu.cn

† Contact author: weili83@tsinghua.edu.cn

reduction contrasting with non-superconducting 2 UC FeSe/ rough PbO_x [Fig. S6(c), (f)]; (4) STS signatures mirroring superconducting 1 UC FeSe/STO, including ± 60 meV DOS depletion [Figs. 2(c), 3(c) and 4(b)]. Since the detailed lattice structures of the three interfaces are distinct, we suggest that the work function differences and the consequent band bending between the monolayer FeSe and the adjacent substrates play leading roles for the charge transfer. The work function of FeSe is 5.1 eV [19], while the work function of PbO_x varies from 4.8 to 5.5 eV, depending on the growth conditions [35]. In our study, Pb atoms are evaporated using a Knudsen cell, while oxygen atoms are supplied by the heating of STO. This process results in an excess of Pb, thereby giving rise to the formation of n-type PbO_x. Consequently, the work function of n-type PbO_x is lower than that of FeSe, allowing electrons to transfer from PbO_x to FeSe [Fig. 4(e)]. This is the case for the monolayer FeSe in Region I. For the monolayer FeSe on the rougher PbO_x area in Region II, comparable charge transfer [see Fig. 2(c) and Fig. 3(c)] and superconducting gaps [see Fig. 2(d) and Fig. 3(g)] are observed, indicating that the two types of PbO_x have similar work functions and the band bending is denoted by the black lines in Fig. 4(e). For the additional monolayer FeSe layers grown on $\sqrt{5} \times \sqrt{5}$ Fe₁₀Se₉, the observed gap size is smaller, suggesting a smaller amount of charge transfer to FeSe, and a higher work function of the insulating $\sqrt{5} \times \sqrt{5}$ Fe₁₀Se₉. And the corresponding band bending is denoted by the gray lines in Fig. 4(e). The hypothesis of charge transfer can be further corroborated by large-scale dI/dV spectra. Spectral hump positions (-240 meV in Region I, -220 meV in II, -140 meV in FeSe/ $\sqrt{5} \times \sqrt{5}$, -130 meV in 2 UC FeSe; Fig. S7 [24]) track electron doping levels via Fe 3d_{z²}-band shifts near the Γ point [3]. Stronger doping in Regions I/II (humps farthest from E_F) correlates with larger superconducting gaps, while slightly doping in FeSe/ $\sqrt{5} \times \sqrt{5}$ yields a reduced "gap-like" feature.

An insulating Se-deficient FeSe structure is not known before. A previous first-principles study on FeSe monolayer with artificial 2×2 Se-vacancy ordering shows a metallic band structure within the

framework of standard density functional theory (DFT) [36]. Our own DFT calculation (shown in the Supplemental Material [24]) based on the experimental $\sqrt{5} \times \sqrt{5}$ Fe₁₀Se₉ superstructure does not find an insulating ground state either [see Figs. S8(a)-(b)]. Nevertheless, introducing antiferromagnetic (AFM) orders to the Fe plane is found to drastically suppress the density of states at the Fermi level, and an additional +U correction to the Fe 3d-orbitals clearly opens a gap [see Figs. S8(c)-(f)]. We have tested both the Néel order [see Fig. S8(c)] and a less regular AFM configuration by arbitrarily assigning 5 Fe spins within the supercell pointing up and the rest pointing down [See Fig. S8(e)]. The gap opening behaviors are qualitatively the same. However, without the AFM order, the +U correction alone is insufficient to drive a metal-to-insulator transition [see Fig. S8(b)]. The scenario appears similar to FeSe with $\sqrt{5} \times \sqrt{5}$ ordered Fe vacancies [37], which has attracted extensive studies because tuning FeSe from a superconductor to an insulator provides a unique angle to understand iron-based superconductors [34,37-41]. Intuitively, the intact Fe plane in the new $\sqrt{5} \times \sqrt{5}$ Fe₁₀Se₉ structure bridges to the superconducting pristine FeSe in a more natural way. Our preliminary calculations suggest that electron correlation plays an important role in opening the insulating gap. The same correlation might also underpin the superconducting phase. While a thorough understanding calls for further study, we believe that this new insulating phase contains novel clues for a deeper insight and further optimization of high-temperature superconductivity.

ACKNOWLEDGMENTS

The research was supported by the National Science Foundation of China (Grants Nos. 92365201, 52388201, 12374062), the Ministry of Science and Technology of China (Grant No. 2022YFA1403100), and the Innovation Program for Quantum Science and Technology (2021ZD0302400).

-
- [1] Q.-Y. Wang, Z. Li, W.-H. Zhang, Z.-C. Zhang, J.-S. Zhang, W. Li, H. Ding, Y.-B. Ou, P. Deng, and K. Chang, Interface-induced high-temperature superconductivity in single unit-cell FeSe films on SrTiO₃, *Chin. Phys. Lett.* **29**, 037402 (2012).
 [2] S. He, J. He, W. Zhang, L. Zhao, D. Liu, X. Liu, D. Mou, Y.-B. Ou, Q.-Y. Wang, and Z. Li, Phase

- diagram and electronic indication of high-temperature superconductivity at 65 K in single-layer FeSe films, *Nat. Mater.* **12**, 605 (2013).
 [3] S. Tan, Y. Zhang, M. Xia, Z. Ye, F. Chen, X. Xie, R. Peng, D. Xu, Q. Fan, and H. Xu, Interface-induced superconductivity and strain-dependent spin density waves in FeSe/SrTiO₃ thin films, *Nat. Mater.* **12**, 634 (2013).

*Contact author: qkxue@mail.tsinghua.edu.cn

† Contact author: weili83@tsinghua.edu.cn

- [4] C.-L. Song, H.-M. Zhang, Y. Zhong, X.-P. Hu, S.-H. Ji, L. Wang, K. He, X.-C. Ma, and Q.-K. Xue, Observation of double-dome superconductivity in potassium-doped FeSe thin films, *Phys. Rev. Lett.* **116**, 157001 (2016).
- [5] T. Ying, M. Wang, X. Wu, Z. Zhao, Z. Zhang, B. Song, Y. Li, B. Lei, Q. Li, and Y. Yu, Discrete superconducting phases in FeSe-derived superconductors, *Phys. Rev. Lett.* **121**, 207003 (2018).
- [6] Y. Xu, H. Rong, Q. Wang, D. Wu, Y. Hu, Y. Cai, Q. Gao, H. Yan, C. Li, and C. Yin, Spectroscopic evidence of superconductivity pairing at 83 K in single-layer FeSe/SrTiO₃ films, *Nat. Commun.* **12**, 2840 (2021).
- [7] Y. Zhang, M. Yi, Z.-K. Liu, W. Li, J. Lee, R. Moore, M. Hashimoto, M. Nakajima, H. Eisaki, and S.-K. Mo, Distinctive orbital anisotropy observed in the nematic state of a FeSe thin film, *Phys. Rev. B* **94**, 115153 (2016).
- [8] W. Li, Y. Zhang, P. Deng, Z. Xu, S.-K. Mo, M. Yi, H. Ding, M. Hashimoto, R. Moore, and D.-H. Lu, Stripes developed at the strong limit of nematicity in FeSe film, *Nat. Phys.* **13**, 957 (2017).
- [9] Y. Yuan, X. Fan, X. Wang, K. He, Y. Zhang, Q.-K. Xue, and W. Li, Incommensurate smectic phase in close proximity to the high- T_c superconductor FeSe/SrTiO₃, *Nat. Commun.* **12**, 2196 (2021).
- [10] R. Peng, H. Xu, S. Tan, H. Cao, M. Xia, X. Shen, Z. Huang, C. Wen, Q. Song, and T. Zhang, Tuning the band structure and superconductivity in single-layer FeSe by interface engineering, *Nat. Commun.* **5**, 5044 (2014).
- [11] X. Fan, W. Cui, Y. Yuan, Q.-K. Xue, and W. Li, Ubiquitous stripe phase and enhanced electron pairing in the interfacial high- T_c superconductor FeSe/BaTiO₃, *Phys. Rev. B* **106**, 024517 (2022).
- [12] H. Ding, Y.-F. Lv, K. Zhao, W.-L. Wang, L. Wang, C.-L. Song, X. Chen, X.-C. Ma, and Q.-K. Xue, High-temperature superconductivity in single-unit-cell FeSe films on anatase TiO₂(001), *Phys. Rev. Lett.* **117**, 067001 (2016).
- [13] G. Zhou, Q. Zhang, F. Zheng, D. Zhang, C. Liu, X. Wang, C.-L. Song, K. He, X.-C. Ma, and L. Gu, Interface enhanced superconductivity in monolayer FeSe films on MgO (001): charge transfer with atomic substitution, *Sci. Bull.* **63**, 747 (2018).
- [14] H. Yang, G. Zhou, Y. Zhu, G.-M. Gong, Q. Zhang, M. Liao, Z. Li, C. Ding, F. Meng, and M. Rafique, Superconductivity above 28 K in single unit cell FeSe films interfaced with GaO_{2-δ} layer on NdGaO₃(110), *Sci. Bull.* **64**, 490 (2019).
- [15] Y. Song, Z. Chen, Q. Zhang, H. Xu, X. Lou, X. Chen, X. Xu, X. Zhu, R. Tao, and T. Yu, High temperature superconductivity at FeSe/LaFeO₃ interface, *Nat. Commun.* **12**, 5926 (2021).
- [16] D. Liu, W. Zhang, D. Mou, J. He, Y.-B. Ou, Q.-Y. Wang, Z. Li, L. Wang, L. Zhao, and S. He, Electronic origin of high-temperature superconductivity in single-layer FeSe superconductor, *Nat. Commun.* **3**, 931 (2012).
- [17] J. Lee, F. Schmitt, R. Moore, S. Johnston, Y.-T. Cui, W. Li, M. Yi, Z. Liu, M. Hashimoto, and Y. Zhang, Interfacial mode coupling as the origin of the enhancement of T_c in FeSe films on SrTiO₃, *Nature* **515**, 245 (2014).
- [18] J. Bang, Z. Li, Y. Y. Sun, A. Samanta, Y. Y. Zhang, W. Zhang, L. Wang, X. Chen, X. Ma, Q. K. Xue, and S. B. Zhang, Atomic and electronic structures of single-layer FeSe on SrTiO₃(001): The role of oxygen deficiency, *Phys. Rev. B* **87**, 220503 (2013).
- [19] H. Zhang, D. Zhang, X. Lu, C. Liu, G. Zhou, X. Ma, L. Wang, P. Jiang, Q.-K. Xue, and X. Bao, Origin of charge transfer and enhanced electron-phonon coupling in single unit-cell FeSe films on SrTiO₃, *Nat. Commun.* **8**, 214 (2017).
- [20] J. P. Perdew, K. Burke, and M. Ernzerhof, Generalized gradient approximation made simple, *Phys. Rev. Lett.* **77**, 3865 (1996).
- [21] S. L. Dudarev, G. A. Botton, S. Y. Savrasov, C. J. Humphreys, and A. P. Sutton, Electron-energy-loss spectra and the structural stability of nickel oxide: An LSDA+U study, *Phys. Rev. B* **57**, 1505 (1998).
- [22] P. E. Blöchl, O. Jepsen, and O. K. Andersen, Improved tetrahedron method for Brillouin-zone integrations, *Phys. Rev. B* **49**, 16223 (1994).
- [23] K. Szot, W. Speier, R. Carius, U. Zastrow, and W. Beyer, Localized metallic conductivity and self-healing during thermal reduction of SrTiO₃, *Phys. Rev. Lett.* **88**, 075508 (2002).
- [24] See Supplemental Material at [URL will be inserted by publisher] for further details and additional supporting data.
- [25] L. Zhang, F. Guo, X. Liu, J. Cui, and Y. Qian, Metastable PbO crystal grown through alcohol-thermal process, *J. Cryst. Growth* **280**, 575 (2005).
- [26] A. Netzahual-Lopantzi, L. Juárez-Santacruz, E. García-Nieto, J. L. Jiménez-Pérez, I. C. Romero-Ibarra, U. O. García-Vidal, and A. Cruz-Orea, Study of the thermal diffusivity and optical properties of lead oxide nanoparticles annealed at different temperatures, *Int. J. Thermophysics* **43**, 86 (2022).

*Contact author: qkxue@mail.tsinghua.edu.cn

†Contact author: weili83@tsinghua.edu.cn

- [27] P. Kumar, J. Liu, P. Ranjan, Y. Hu, S. S. Yamijala, S. K. Pati, J. Irudayaraj, and G. J. Cheng, Alpha lead oxide (α -PbO): a new 2D material with visible light sensitivity, *Small* **14**, 1703346 (2018).
- [28] S. Venkataraj, J. Geurts, H. Weis, O. Kappertz, W. K. Njoroge, R. Jayavel, and M. Wuttig, Structural and optical properties of thin lead oxide films produced by reactive direct current magnetron sputtering, *J. Vac. Sci. Technol. A* **19**, 2870 (2001).
- [29] C. Ding, Z. Wei, W. Dong, H. Feng, M. Shi, L. Wang, J.-F. Jia, and Q.-K. Xue, Atomic-site-dependent pairing gap in monolayer FeSe/SrTiO₃ (001)-($\sqrt{13} \times \sqrt{13}$), *Nano Lett.* **24**, 8445 (2024).
- [30] X. Jiao, G. Gong, Z. Zhang, W. Dong, C. Ding, M. Pan, L. Wang, and Q.-K. Xue, Post-growth Fe deposition on the superconductivity of monolayer FeSe films on SrTiO_{3- δ} , *Phys. Rev. Mater.* **6**, 064803 (2022).
- [31] Y. Hu, Y. Xu, Y.-M. Zhang, Q. Wang, S. He, D. Liu, A. Liang, J. Huang, C. Li, and Y. Cai, Discovery of an insulating parent phase in single-layer FeSe/SrTiO₃ films, *Phys. Rev. B* **102**, 115144 (2020).
- [32] G. Gong, H. Yang, Q. Zhang, C. Ding, J. Zhou, Y. Chen, F. Meng, Z. Zhang, W. Dong, and F. Zheng, Oxygen vacancy modulated superconductivity in monolayer FeSe on SrTiO_{3- δ} , *Phys. Rev. B* **100**, 224504 (2019).
- [33] H. Zhang, Z. Ge, M. Weinert, and L. Li, Sign changing pairing in single layer FeSe/SrTiO₃ revealed by nonmagnetic impurity bound states, *Commun. Phys.* **3**, 75 (2020).
- [34] W. Li, H. Ding, Z. Li, P. Deng, K. Chang, K. He, S. Ji, L. Wang, X. Ma, J.-P. Hu, X. Chen, and Q.-K. Xue, KFe₂Se₂ is the parent compound of K-doped iron selenide superconductors, *Physical Review Letters* **109**, 057003 (2012).
- [35] L. Droessler, University of Oxford, 2014.
- [36] T. Berlijn, H.-P. Cheng, P. Hirschfeld, and W. Ku, Doping effects of Se vacancies in monolayer FeSe, *Phys. Rev. B* **89**, 020501 (2014).
- [37] M. Gao, X. Kong, X.-W. Yan, Z.-Y. Lu, and T. Xiang, Pair-checkerboard antiferromagnetic order in β -Fe₄Se₅ with $\sqrt{5} \times \sqrt{5}$ -ordered Fe vacancies, *Phys. Rev. B* **95**, 174523 (2017).
- [38] T.-K. Chen, C.-C. Chang, H.-H. Chang, A.-H. Fang, C.-H. Wang, W.-H. Chao, C.-M. Tseng, Y.-C. Lee, Y.-R. Wu, M.-H. Wen, H.-Y. Tang, F.-R. Chen, M.-J. Wang, M.-K. Wu, and D. Van Dyck, Fe-vacancy order and superconductivity in tetragonal β -Fe_{1-x}Se, *Proc. Natl. Acad. Sci. U.S.A* **111**, 63 (2014).
- [39] K.-Y. Yeh, Y.-R. Chen, T.-S. Lo, P. M. Wu, M.-J. Wang, K.-S. Chang-Liao, and M.-K. Wu, Fe-Vacancy-Ordered Fe₄Se₅: The Insulating Parent Phase of FeSe Superconductor, *Front. Phys.* **8** (2020).
- [40] W. Zhang, Z. M. Zhang, J. H. Nie, B. C. Gong, M. Cai, K. Liu, Z. Y. Lu, and Y. S. Fu, Spin-resolved imaging of antiferromagnetic order in Fe₄Se₅ ultrathin films on SrTiO₃, *Adv. Mater.* **35**, 2209931 (2023).
- [41] C.-L. Xue, L.-G. Dou, Y.-J. Xu, Q.-Q. Yuan, Q.-Y. Li, Z.-Y. Jia, Z. Li, R. Liu, and S.-C. Li, Iron vacancy tunable superconductor-insulator transition in FeSe/SrTiO₃ monolayer, *Phys. Rev. Lett.* **131**, 256002 (2023).

*Contact author: qkxue@mail.tsinghua.edu.cn

† Contact author: weili83@tsinghua.edu.cn